Global monitoring of fluidized-bed processes by means of microwave cavity resonances

Measurement 55 (2014) 520–535

Contents lists available at ScienceDirect

Measurement

journal homepage: www.elsevier.com/locate/measurement

Global monitoring of fluidized-bed processes by means of microwave cavity resonances

Johan Nohlert [a,*], Livia Cerullo [a], Johan Winges [a], Thomas Rylander [a], Tomas McKelvey [a], Anders Holmgren [b], Lubomir Gradinarsky [b], Staffan Folestad [b], Mats Viberg [a], Anders Rasmuson [c]

[a] Department of Signals and Systems, Chalmers University of Technology, SE-41296 Göteborg, Sweden
[b] AstraZeneca R&D, Pharmaceutical Development, SE-431 83 Mölndal, Sweden
[c] Department of Chemical and Biological Engineering, Chalmers University of Technology, SE-41296 Göteborg, Sweden

ARTICLE INFO

Article history:
Received 16 October 2013
Accepted 23 May 2014
Available online 19 June 2014

Keywords:
Pharmaceutical fluidized-bed process
Microwave measurement system
Permittivity estimation
Electromagnetic homogenization
Finite element method
Sensitivity analysis

ABSTRACT

We present an electromagnetic measurement system for monitoring of the effective permittivity in closed metal vessels, which are commonly used in the process industry. The measurement system exploits the process vessel as a microwave cavity resonator and the relative change in its complex resonance frequencies is related to the complex effective permittivity inside the vessel. Also, thermal expansion of the process vessel is taken into account and we compensate for its influence on the resonance frequencies by means of a priori information derived from a set of temperature measurements. The sensitivities, that relate the process state to the measured resonance frequencies, are computed by means of a detailed finite element model. The usefulness of the proposed measurement system is successfully demonstrated for a pharmaceutical fluidized-bed process, where the water and solid contents inside the process vessel is of interest.

1. Introduction

In the pharmaceutical industry, monitoring and control of manufacturing processes are important in order to achieve high-quality products to a low production-cost. A common step in the manufacturing process for many pharmaceutical products is coating and drying of particles in fluidized-bed processes. Measurement techniques that are capable of monitoring the material distribution and moisture content in this type of process are important tools for control, optimization and improved understanding of the process.

Currently available methods for monitoring of moisture content in pharmaceutical fluidized-beds include spectroscopic methods such as near infra-red (NIR) and Raman spectroscopy [1,2]. Although these methods yield important information on moisture content as well as physical and chemical properties of the material, they mainly provide local information for the region in the very proximity of the measurement probe, which may be insufficient or misleading for the estimation of the global process state. Recently, Buschmüller et al. [3] developed a stray field microwave resonator technique for in-line moisture measurements during fluidized-bed drying. However, their approach is based on local fields in the vicinity of the resonator probe and, therefore, it does not yield global information on the process state.

At low frequencies, electric capacitance tomography (ECT) can be applied to regions with high particle density [4]. Although ECT yields important information on the particle distribution on a global scale, it suffers from limited spatial resolution and it is not suited for the estimation

* Corresponding author. Tel.: +46 317721710.
E-mail address: nohlertj@chalmers.se (J. Nohlert).

http://dx.doi.org/10.1016/j.measurement.2014.05.034
0263-2241/

of dielectric losses, which leads to difficulties in distinguishing between material density and moisture content.

In this article, we present a microwave-based measurement technique that exploits electromagnetic eigenmodes that are supported by the process vessel bounded by its metal walls. The process vessel is considered as a cavity resonator and the permittivity distribution inside the vessel is estimated based on measurements of the complex resonance frequencies of the cavity. This technique resembles the well-established cavity perturbation measurement technique, which is regularly used for accurate measurements of dielectric and magnetic properties of materials at microwave frequencies [5,6]. In contrast to traditional cavity-perturbation measurements, our technique exploits several different eigenmodes, which yields three-dimensional spatial resolution and measurement information at multiple frequencies.

The process vessel is equipped with a set of probes that are connected to a network analyzer. Given the scattering parameters measured with the network analyzer, we estimate the complex resonance frequencies of the process vessel, where the real part corresponds to the frequency of oscillation and the imaginary part corresponds to the damping. We exploit a linearization of the electromagnetic response of the process vessel and it yields a relation between (i) a perturbation of the resonance frequencies and (ii) a perturbation of the complex permittivity inside the process vessel. We parameterize the permittivity with space dependent basis functions and determine the coefficients by means of solving an estimation problem based on an over-determined system of linear equations, where the right-hand side contains the measured deviations in the resonance frequencies as compared to the empty vessel.

2. Measurement system

2.1. Process equipment

Fig. 1 shows a schematic picture of a fluidized-bed process vessel of Wurster type, which is the type of process we consider in this article. This process is used for coating and drying of pharmaceutical particles, such as pellets or granules, and the particular vessel we consider is a custom built lab-scale device for batches consisting of up to 1 kg of particles. The particles are dielectric objects of size that normally range from 250 μm to 1 mm and in this article, we consider particles that mainly consist of microcrystalline cellulose (MCC).

The bottom plate of the process vessel, also referred to as the distributor plate, is perforated with a large number of small holes. An airflow is applied through the distributor plate, which fluidizes the particles and creates a fluidized bed. Above the distributor plate resides a metal tube, which is referred to as the Wurster tube. At the center of the distributor plate below the Wurster tube, a pneumatic spray nozzle injects a rapidly moving mixture of air and liquid that accelerates the particles in its immediate vicinity in an upward motion. The particles move through the Wurster tube and create a fountain-like flow pattern above the Wurster tube. As the particles exit the fountain region, they fall back into the fluidized bed outside the Wurster tube.

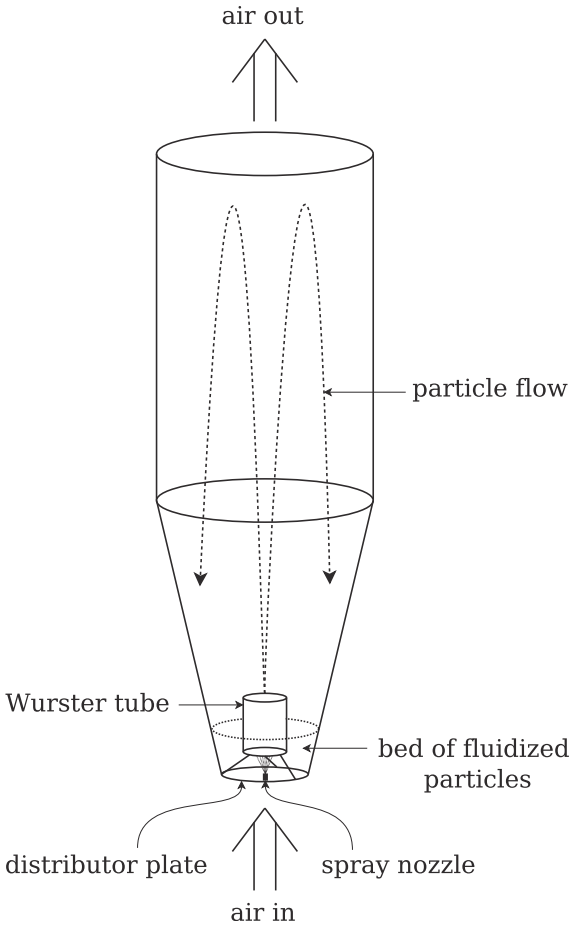

Fig. 1. Schematic picture of the process vessel.

The liquid injected through the spray nozzle is a solution that is sprayed onto the surface of the particles. The solvent evaporates mainly inside and immediately above the Wurster tube, which results in a deposited layer of the solute on the surface of the particles [7]. A common solvent is water and there is a large variety of solutes such as active pharmaceutical ingredients (API), polymers used for film coating and various filler materials. Thus, this type of process allows for the manufacturing of multi-layered particles. Here, the different layers provide designed functions such as protection from humidity during storage, delay of API release in the digestive system and the actual delivery of the API.

The water and its distribution inside the vessel for the duration of the process influence the process state and, consequently, the quality of the final product. For example, API that are sensitive to long-term exposure to moisture may be coated with a film that protects the API from ambient humidity. In such cases, it is important to establish that the particles are sufficiently dry before this film is applied. In addition, a too fast drying rate may have negative impact on the coating quality. A more extreme situation is the undesirable event of excessive amounts of water inside the vessel, which can cause extensive particle

agglomeration and eventually process break-down. If such a condition can be detected, it is feasible to change the process parameters in order to counter-act agglomeration. The water inside the vessel can occur in a number of different forms: (i) water vapor; (ii) sorbed water inside the particles; (iii) free water on the surface of the particles; (iv) water droplets in the air; (v) condensed water droplets on the vessel walls; and (vi) water in agglomerates or dense gatherings of particles.

2.2. Measurement principle

From an electromagnetic point of view, the process vessel that we consider is a rather good approximation of a microwave cavity resonator. The geometry of the vessel, which is used in the electromagnetic model described later in the article, is shown in Fig. 2. We exploit two magnetic-field probes to excite eigenmodes supported by the microwave resonator and the corresponding eigenfrequencies are measured with the same set of probes. A network analyzer is connected to the two probes and the 2×2 scattering matrix is measured as a function of frequency. The measured scattering parameters are used to extract the complex resonance frequencies of a selection of the lowest eigenmodes supported by the process vessel.

It should be emphasized that although these probes are rather small in comparison to the microwave resonator, i.e., the process vessel, the electromagnetic field for basically all eigenmodes extends throughout most of the process vessel's volume. The eigenfrequencies are influenced by the geometry of the process vessel and, more importantly for this application, the material and its distribution inside the process vessel. Consequently, important information on the distribution of particles and their moisture content can be derived from the measured eigenfrequencies.

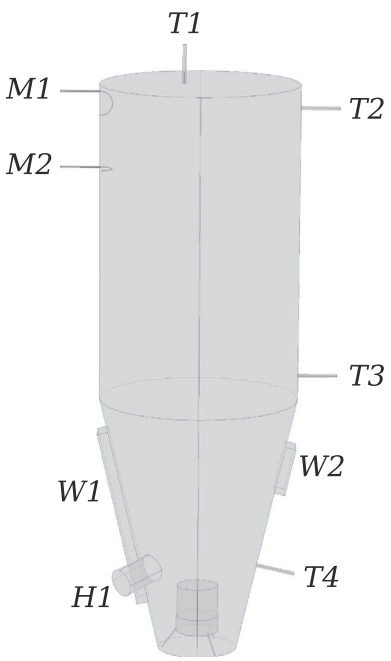

Fig. 2. The process vessel including its two rectangular windows (W1 and W2) and the cylindrical tube used for loading of particles (H1). This figure also illustrates four temperature probes (T1–T4) and two microwave probes (M1 and M2) although these are not part of the electromagnetic model.

2.2.1. Homogenization of a mixture of air and particles

The mixture of particles and air influences the electromagnetic fields inside the process vessel. The typical length-scales associated with the lowest eigenmodes are comparable to the size of the cavity and, as a consequence, the particles are extremely small in relation to the spatial variation of the electromagnetic field. Thus, it is beneficial to represent the mixture of particles and air in terms of an effective permittivity, where the possible presence of other small dielectric objects, such as liquid droplets, contributes to the effective permittivity in the same manner as the particles. Given the material parameters and geometry of the particles together with their spatial distribution, the effective permittivity can be calculated by means of electromagnetic mixing formulas [8]. Here, we focus on the well-known Maxwell–Garnett mixing formula

$$\frac{\epsilon_{\text{eff}} - \epsilon_{\text{b}}}{\epsilon_{\text{eff}} + 2\epsilon_{\text{b}}} = \frac{1}{3\epsilon_{\text{b}}} \sum_{n=1}^{N} \vartheta_n \frac{\alpha_n}{V_n}, \tag{1}$$

where ϵ_{eff} is the effective permittivity and ϵ_{b} is the permittivity of the background medium for a mixture with N different types of inclusions indexed by n. In this article, we assume that ϵ_{b} is real, i.e., we have a lossless background medium. For the inclusions of type n, we have the polarizability α_n, the inclusion volume V_n and the volume fraction ϑ_n. For homogeneous spherical inclusions with permittivity ϵ_{i}, we have the polarizability

$$\alpha = 3\epsilon_{\text{b}} V \frac{\epsilon_{\text{i}} - \epsilon_{\text{b}}}{\epsilon_{\text{i}} + 2\epsilon_{\text{b}}}, \tag{2}$$

where V is the volume of the particle. Layered spherical particles with a core and an outer shell with different permittivities can also be incorporated into Eq. (1) by using the associated polarizability for this type of inclusions [8].

A dispersive inclusion material yields a dispersive behavior of the effective permittivity, although the dispersion relation of the mixture may be different from that of the inclusions. For example, air with inclusions that are described as a Debye medium yields an effective permittivity that also behaves like a Debye medium, but with different values of the Debye parameters [9]. Furthermore, air and inclusion particles with non-zero conductivity yields Debye-characteristics of the effective permittivity, due to the Maxwell–Wagner effect [10].

2.2.2. Density independent moisture measurements

A feasible way to extract information about moisture content of the particles from the estimated complex effective permittivity $\epsilon_{\text{eff}} = \epsilon'_{\text{eff}} - j\epsilon''_{\text{eff}}$ in the process vessel, is the approach of density-independent measurement techniques [10]. The main idea of this approach is that if the material density in a given volume changes, both ϵ'_{eff} and ϵ''_{eff} will be affected in a similar way, since they both

depend on the total amount of polarizable material in the volume.

In a situation where a certain material is dispersed in a background medium with permittivity ϵ_b, the ratio

$$\eta = \frac{\epsilon''_{eff}}{\epsilon'_{eff} - \epsilon_b}, \tag{3}$$

is an example of a density-independent function that has shown to be more or less independent on the density for many material mixtures [11,12]. This is not surprising, and it can be shown using the Maxwell–Garnett mixing formula applied to lossy spherical inclusions dispersed in a lossless background medium, that η is independent on the volume fraction ϑ in the low-density limit. Therefore, it is expected that measurements of ϵ''_{eff} and ϵ'_{eff} taken at different material densities would fall on a straight line that intersects the origin if ϵ''_{eff} is plotted versus $\epsilon'_{eff} - \epsilon_b$, given that the particles have constant permittivity. The slope η of this line usually depends on the moisture content of the inclusion material in a characteristic manner. The slope η may therefore be used as a density-independent metric of the moisture content, if it is known how η depends on the moisture content for the material considered. Such relations are usually obtained from calibration procedures which involve measurements on material samples with known moisture content. It should be emphasized that η may depend on many other factors as well, such as the physical state of the water (e.g. whether it is free or bound in the material) and the temperature. In the case of free water, its distribution in the material may also be of importance.

In practical measurement situations, the estimated effective permittivity ϵ_{eff} may be biased by, e.g., temperature variations of the metal parts of the cavity, or by changes in the permittivity of the background medium (which is usually air) caused by, e.g., a varying humidity. In such cases, there may be non-zero residual components of ϵ''_{eff} and $\epsilon'_{eff} - \epsilon_b$ at zero material density due to biased estimates of ϵ_{eff}, which makes a direct use of the ratio η unreliable. We therefore make an attempt to extend the classical density-independent measurement approach to situations where an uncontrolled bias of the estimated ϵ_{eff} is present. Our approach is based on the covariance between ϵ''_{eff} and $\epsilon'_{eff} - \epsilon_b$, which is computed for a fairly large number of measurement samples. The material (in our case the particles in the process) is re-distributed between different sample points which yields a variation in the material density and hence a variation in ϵ''_{eff} and ϵ'_{eff}, which is used to calculate the covariance. As a motivation to this approach, we consider a situation where lossy spherical inclusions with permittivity $\epsilon_i = \epsilon'_i - j\epsilon''_i$ are dispersed in a background medium with permittivity ϵ_b with volume fraction ϑ. If the dispersion is dilute ($\vartheta \ll 1$) and if the loss factor of the inclusion material is low ($\epsilon''_i/\epsilon'_i \leqslant 0.1$), the Maxwell–Garnett mixing formula yields the following expressions for the real and imaginary parts of the effective permittivity

$$\epsilon'_{eff}/\epsilon_b - 1 \simeq 3\frac{\epsilon'_i/\epsilon_b - 1}{\epsilon'_i/\epsilon_b + 2}\vartheta \tag{4}$$

$$\epsilon''_{eff}/\epsilon_b \simeq 9\frac{\epsilon''_i/\epsilon_b}{(\epsilon'_i/\epsilon_b + 2)^2}\vartheta. \tag{5}$$

If we now assume that ϑ, ϵ'_i and ϵ''_i vary randomly around their respective mean values, this will obviously yield variations in ϵ_{eff}. Hence, by studying the covariance between the real and imaginary part of ϵ_{eff}, one may extract important information about the parameters ϑ, ϵ'_i and ϵ''_i and their variabilities. In particular, we notice from Eqs. (4) and (5) that both the real and imaginary part of ϵ_{eff} depend linearly on the volume fraction ϑ, which explains the density-independent nature of the ratio η and the reason why ϵ''_{eff} and $\epsilon'_{eff} - \epsilon_b$ obtained from different volume fractions tend to fall on a straight line. Deviations from this line can be explained by means of variations in ϵ'_i and ϵ''_i, since they influence the real and imaginary part of ϵ_{eff} in different ways, as seen from Eqs. (4) and (5).

2.3. Experimental setup

The experimental setup is shown in Fig. 3a and it includes the process vessel, the process machine and the two-port network analyzer used to perform the microwave measurements.

2.3.1. Reduction of undesired losses

The original process vessel has a couple of apertures, such as windows that are used for visual inspection of the process, and such apertures damp the microwave cavity by means of radiation losses. We are interested in measuring the damping associated with the moisture content of the particles and, thus, we wish to reduce other contributions to the total damping of the cavity. Therefore, we shield the process vessel by covering the apertures W1, W2 and H1 in Fig. 2 by aluminum foil, and use a perforated plate to shield the microwave cavity from the air outtake in the upper part of the process vessel. In addition, the shielding mitigates possible problems with external electromagnetic sources that may disturb the measurements. With these arrangements we obtain unloaded Q-values of the cavity which are in the order of 10^3–10^4 for the lowest eigenmodes.

2.3.2. Choice of probes and their design

Pharmaceutical mixtures processed in steel containers often become electrically charged due to the triboelectric effect [13,14]. Consequently, the statically charged particles yield a quasi-static electric field as they move inside the vessel. In order to protect the network analyzer from induced voltages of large magnitude and electric discharges that may occur in the process vessel, we exploit magnetic field probes (also referred to as H-probes) that are mainly sensitive to the time variations of the magnetic flux that passes through the loop of the H-probe.

Fig. 3b shows the process vessel equipped with two H-probes located in the upper part of the cavity for measurement of the azimuthal and vertical components of the magnetic field. At these locations, we can efficiently couple to the magnetic field of the lowest eigenmodes that we use for sensing. In addition, the size of each loop is chosen such that we get sufficiently good coupling to all of these modes. For industrial usage, it may not be feasible to let the probe extend into the process vessel. A possible remedy is to

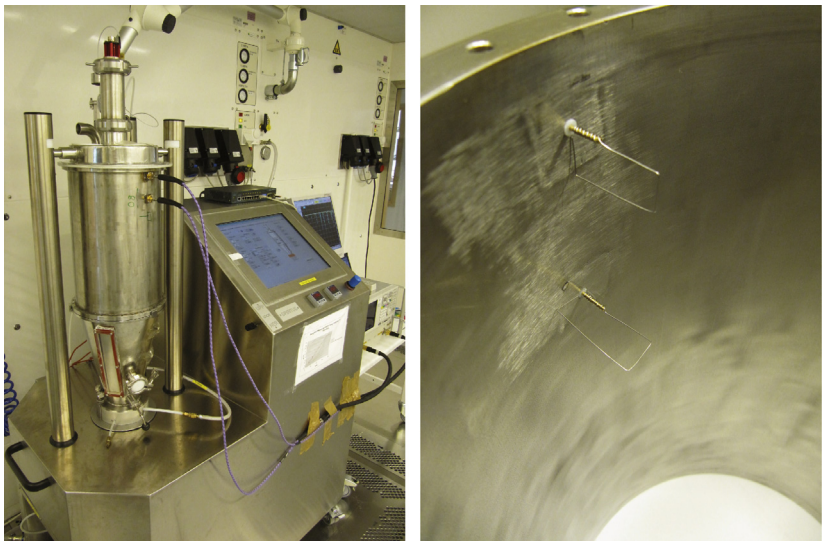

(a) Experimental setup (b) H-probes

Fig. 3. Photographs of (a) the process vessel in the experimental setup and (b) the two H-probes.

create a shallow dent in the cavity wall and to cover this dent by a dielectric "radome".

2.3.3. Measurement settings

The network analyzer (Agilent E8361A) is controlled from a PC via GPIB interface, in order to perform repeated scans of a frequency band that includes the resonance frequencies of the sensing modes (0.7–1.7 GHz). This frequency band takes approximately 2 s to scan (for excitation on one of the two ports), using totally 6400 frequency points and the IF bandwidth set to 5 kHz, which means that it takes 1–10 ms to scan the frequency band occupied by a single resonance. The time between two consecutive frequency sweeps is set to 10 s, where a substantial part of this time is required for data transfer over the GPIB interface. In the post-processing of the measurement data, we use a statistical approach which benefits from a large number of measurement samples. Therefore, a measurement setup that allows for faster sampling of the process would be beneficial for this measurement technique.

3. Electromagnetic model

For the analysis of the resonance frequencies and the corresponding eigenmodes, we use an idealized model of the process vessel: (i) all the metal parts of the process vessel are assumed to be perfect electric conductors (PEC); (ii) all apertures are completely sealed such that the interior of the process vessel is completely enclosed by a perfect electric conductor; and (iii) the probes are excluded from the model. Further, we assume that the material inside the process vessel can be described by relatively simple dispersion relations for the frequency band of interest and, as a starting point, we consider a frequency-independent permittivity that may vary with respect to space. Also, we assume that the magnetization for the media involved is negligible and use the permeability $\mu = \mu_0$.

Thus, we consider the eigenvalue problem

$$\nabla \times \boldsymbol{E} = -j\omega \boldsymbol{B} \text{ in } \Omega, \tag{6}$$

$$\nabla \times \frac{1}{\mu_0}\boldsymbol{B} = (j\omega\epsilon + \sigma)\boldsymbol{E} \text{ in } \Omega, \tag{7}$$

$$\hat{\boldsymbol{n}} \times \boldsymbol{E} = 0 \text{ on } \Gamma. \tag{8}$$

We seek the eigenmodes $(\boldsymbol{E}_m, \boldsymbol{B}_m)$ and the corresponding eigenfrequencies ω_m that satisfy the eigenvalue problem (6)–(8), where the index m labels the resonances supported by the process vessel.

3.1. Weak formulation

The eigenvalue problem (6)–(8) is expressed in the weak form: Find $(\boldsymbol{E}, \boldsymbol{B}, \omega) \in H_0(\text{curl}; \Omega) \times H(\text{div}; \Omega) \times \mathbb{C}$ such that

$$c_{\text{FL}}(\boldsymbol{E}, \boldsymbol{v}) = -j\omega m_1(\boldsymbol{B}, \boldsymbol{v}), \tag{9}$$

$$c_{\text{AL}}(\boldsymbol{B}, \boldsymbol{w}) = j\omega\mu_0\epsilon_0 m_{\epsilon_r}(\boldsymbol{E}, \boldsymbol{w}) + \mu_0 m_\sigma(\boldsymbol{E}, \boldsymbol{w}), \tag{10}$$

for all $(\boldsymbol{v}, \boldsymbol{w}) \in H(\text{div}; \Omega) \times H_0(\text{curl}; \Omega)$. Here, we express the real (absolute) permittivity $\epsilon = \epsilon_0\epsilon_r$ in terms of the corresponding relative permittivity. Further, we have the bilinear forms

$$c_{\text{FL}}(\boldsymbol{u}, \boldsymbol{v}) = \int_\Omega (\nabla \times \boldsymbol{u}) \cdot \boldsymbol{v}\, d\Omega, \tag{11}$$

$$c_{\text{AL}}(\boldsymbol{u}, \boldsymbol{v}) = \int_\Omega \boldsymbol{u} \cdot (\nabla \times \boldsymbol{v})\, d\Omega, \tag{12}$$

$$m_1(\boldsymbol{u}, \boldsymbol{v}) = \int_\Omega \boldsymbol{u} \cdot \boldsymbol{v}\, d\Omega, \tag{13}$$

$$m_{\epsilon_r}(\boldsymbol{u}, \boldsymbol{v}) = \int_\Omega \epsilon_r \boldsymbol{u} \cdot \boldsymbol{v}\, d\Omega, \tag{14}$$

$$m_\sigma(\boldsymbol{u}, \boldsymbol{v}) = \int_\Omega \sigma \boldsymbol{u} \cdot \boldsymbol{v}\, d\Omega. \tag{15}$$

Finally, we have the spaces

$$H(\mathrm{curl};\Omega)=\{\boldsymbol{u}:\boldsymbol{u}\in L_2(\Omega)\text{ and }\nabla\times\boldsymbol{u}\in L_2(\Omega)\},\tag{16}$$

$$H(\mathrm{div};\Omega)=\{\boldsymbol{u}:\boldsymbol{u}\in L_2(\Omega)\text{ and }\nabla\cdot\boldsymbol{u}\in L_2(\Omega)\},\tag{17}$$

and $H_0(\mathrm{curl};\Omega)$ is the subspace of $H(\mathrm{curl};\Omega)$ that satisfies the boundary condition (8).

3.2. Finite element approximation

We expand the electric field in terms of curl-conforming elements and the magnetic flux density in divergence-conforming elements, see Ref. [15] for further details. This yields the discrete eigenvalue problem

$$\begin{bmatrix}\mathbf{0} & -\mathbf{C}\\ \mathbf{C}^{\mathrm{T}} & -Z_0\mathbf{M}_\sigma\end{bmatrix}\begin{bmatrix}c_0\mathbf{b}\\ \mathbf{e}\end{bmatrix}=\frac{j\omega}{c_0}\begin{bmatrix}\mathbf{M}_1 & \mathbf{0}\\ \mathbf{0} & \mathbf{M}_{\epsilon_r}\end{bmatrix}\begin{bmatrix}c_0\mathbf{b}\\ \mathbf{e}\end{bmatrix},\tag{18}$$

where we have scaled the magnetic flux density with the speed of light and Ampère's law with the impedance of vacuum. This form is useful since it yields an eigenvalue problem that is linear in terms of the eigenvalue $j\omega/c_0$. Reference [16] contains further details on the treatment of eigenvalue problems by means of the finite element method.

Elimination of the magnetic flux density from Eq. (18) yields the corresponding eigenvalue problem

$$\left(\mathbf{C}^{\mathrm{T}}\mathbf{M}_1^{-1}\mathbf{C}+j\omega\mu_0\mathbf{M}_\sigma-\omega^2\mu_0\epsilon_0\mathbf{M}_{\epsilon_r}\right)\mathbf{e}=\mathbf{0},\tag{19}$$

formulated in terms of only the electric field. This eigenvalue problem is nonlinear since it is quadratic in terms of the eigenfrequency ω.

For problems with conducting media, it is computationally advantageous to solve Eq. (18). Such situations may occur in pharmaceutical processes that feature solutions with ions. For dry processes, the non-conducting background medium with possibly conducting inclusions, displays a more complicated dispersion for the effective permittivity. Given the somewhat limited frequency-band used for the measurements in this article, we choose to approximate the effective permittivity by a frequency-independent function $\epsilon(\boldsymbol{r})=\epsilon'(\boldsymbol{r})-j\epsilon''(\boldsymbol{r})$. This yields the eigenvalue problem

$$\left(\mathbf{C}^{\mathrm{T}}\mathbf{M}_1^{-1}\mathbf{C}-\omega^2\mu_0(\mathbf{M}_{\epsilon'}-j\mathbf{M}_{\epsilon''})\right)\mathbf{e}=\mathbf{0},\tag{20}$$

which is not particularly attractive for direct computation but useful for the sensitivity analysis that follows below.

3.3. Losses due to finite conductivity in the cavity walls

It is possible to approximately determine the losses due to cavity walls of finite conductivity based on the electromagnetic field solution computed for a PEC boundary. This type of approach yields the quality factor associated with a particular eigenmode and, consequently, its damping [17]. The losses are given by

$$P_{\mathrm{wall}}=\mathrm{Re}\left\{\frac{1}{2}\int_\Gamma Z_\Gamma|\hat{\boldsymbol{n}}\times\frac{\boldsymbol{B}_m}{\mu_0}|^2d\Gamma\right\},\tag{21}$$

where $Z_\Gamma=(1+j)/(\sigma\delta_m)$ is the surface impedance for the wall of finite conductivity. Here, $\delta_m=(2/(\omega_m\mu_0\sigma))^{1/2}$ is the penetration depth for the eigenfrequency ω_m and the magnetic flux density $\boldsymbol{B}_m$ of the corresponding eigenmode is computed based on the approximation that the wall conductivity is infinite. Finally, the quality factor is given by $Q_{\mathrm{wall},m}=\omega_m W_m/P_{\mathrm{wall},m}$ where W_m is the time-average energy stored in the vessel by the eigenmode $(\boldsymbol{E}_m,\boldsymbol{B}_m)$, i.e.,

$$W_m=\frac{1}{4}\int_\Omega\epsilon|\boldsymbol{E}_m|^2d\Omega+\frac{1}{4}\int_\Omega\frac{1}{\mu_0}|\boldsymbol{B}_m|^2d\Omega.\tag{22}$$

4. Estimation procedure

Given the measured scattering parameters, we estimate the complex resonance frequencies by means of a subspace-based multivariable system identification algorithm [18]. This measurement procedure is repeated in a regular fashion throughout the entire duration of the process time, and in the following, we refer to the estimated resonance frequencies as the measured resonance frequencies. First, the vessel is empty and the measured resonance frequencies are denoted $\bar{\omega}_m^{\mathrm{ref}}$, where the overline denotes a measured quantity. Next, the process vessel is loaded with particles and the subsequent measured resonance frequencies $\bar{\omega}_m$ are used to form the deviations in the resonance frequencies $\Delta\bar{\omega}_m=\bar{\omega}_m-\bar{\omega}_m^{\mathrm{ref}}$. As the process evolves, we exploit the relative deviation $\Delta\bar{\omega}_m/\bar{\omega}_m^{\mathrm{ref}}$ to estimate the state of the process and, later in this section, we present formulas that relate a perturbation in resonance frequency to the corresponding perturbations in (i) the material parameters and (ii) the shape of the vessel due to thermal expansion.

The estimation of the material and shape parameters is based on minimization of the misfit between the measured and computed relative deviations in resonance frequencies. Thus, we wish to minimize the following expression

$$\sum_m\left|\frac{\Delta\omega_m}{\omega_m^{\mathrm{ref}}}-\frac{\Delta\bar{\omega}_m}{\bar{\omega}_m^{\mathrm{ref}}}\right|^2,\tag{23}$$

where $\Delta\omega_m=\omega_m-\omega_m^{\mathrm{ref}}$ is the deviation in the computed resonance frequencies ω_m as compared to the corresponding (computed) result ω_m^{ref} for the empty reference case. The computed resonance frequencies ω_m are functions of the material and shape parameters, and this dependency may be expressed according to

$$\omega_m=\omega_m|_{\mathrm{LP}}+\sum_n\frac{\partial\omega_m}{\partial p_n}|_{\mathrm{LP}}\delta p_n,\tag{24}$$

for small deviations around a certain linearization point, which is denoted by the subscript LP. The empty cavity may be used as linearization point, but if the permittivity inside the vessel deviates substantially from vacuum, it is beneficial to use a linearization point with higher permittivity in certain regions of the vessel. The perturbations δp_n in the parameters with respect to the linearization point, are stored in a vector $\mathbf{x}$ and we compute an estimate $\hat{\mathbf{x}}$ of $\mathbf{x}$ by means of the regularized approach

$$\hat{\mathbf{x}}=\arg\min_{\mathbf{x}}||\mathbf{A}\mathbf{x}-\mathbf{b}||^2+\gamma||\mathbf{L}(\mathbf{x}-\tilde{\mathbf{x}})||^2.\tag{25}$$

Here, the elements of the matrix $\mathbf{A}$ and the right-hand-side vector $\mathbf{b}$ are given by

$$A_{mn} = \frac{1}{\omega_m^{\mathrm{ref}}} \frac{\partial \omega_m}{\partial p_n}|_{\mathrm{LP}} \tag{26}$$

$$b_m = \frac{\Delta \bar{\omega}_m}{\bar{\omega}_m^{\mathrm{ref}}} - \frac{\omega_m|_{\mathrm{LP}} - \omega_m^{\mathrm{ref}}}{\omega_m^{\mathrm{ref}}}. \tag{27}$$

The first term in Eq. (25) resembles a system of linear equations which is over-determined, i.e., the number of rows in $\mathbf{A}$ exceeds the number of columns. Hence, the residual $||\mathbf{Ax} - \mathbf{b}||$ can be used as a metric of how well the column space of $\mathbf{A}$ is able to represent the data vector $\mathbf{b}$. The second term in Eq. (25) is a regularization term, which penalizes solutions $\hat{\mathbf{x}}$ away from a given vector $\tilde{\mathbf{x}}$ using a weighted Euclidean norm. The matrix $\mathbf{L}$ in the regularization term is diagonal with all diagonal elements equal to unity, except for the elements that multiply the shape parameters, which are substantially larger. The balance between the two terms in Eq. (25), i.e., a solution which makes $\mathbf{A}\hat{\mathbf{x}} \approx \mathbf{b}$ and a solution $\hat{\mathbf{x}} \approx \tilde{\mathbf{x}}$, is controlled by the regularization parameter γ. From a Bayesian point of view we can interpret Eq. (25) as the posterior mean estimate of $\mathbf{x}$ under the assumption that the measurement errors in $\mathbf{b}$ are Gaussian distributed, have zero mean and covariance matrix $\varsigma^2\mathbf{I}$ and the parameter vector $\mathbf{x}$ has a Gaussian prior distribution with mean value $\tilde{\mathbf{x}}$ and covariance matrix $(\varsigma^2/\gamma)(\mathbf{L}^{\mathrm{T}}\mathbf{L})^{-1}$ [19].

For normal process conditions, the losses in the process vessel are small and, therefore, we compute the sensitivity matrix $\mathbf{A}$ for linearization points that corresponds to the vessel without losses. Consequently, the permittivity is represented by $\epsilon = \epsilon'_{\mathrm{LP}} + \delta\epsilon' - j\delta\epsilon''$, where ϵ'_{LP} is the permittivity at the linearization point. Here, the perturbations with respect to the linearization point are denoted $\delta\epsilon'$ and $\delta\epsilon''$, which are estimated by means of Eq. (25).

Thus, we use the eigenvalue problem (20) with $\epsilon'(\boldsymbol{r}) \geqslant \epsilon_0$ and $\epsilon''(\boldsymbol{r}) = 0$ to compute the eigenfrequencies and eigenmodes at the linearization point, which reduces to a special case of Eq. (18). The computed eigenfrequencies and eigenmodes are also used to compute the sensitivities as described later in this section. The down-bed region with the fluidized particles yields an effective permittivity that deviates substantially from vacuum. Therefore, we use a linearization point

$$\epsilon'_{\mathrm{LP}}(\boldsymbol{r}) = \begin{cases} \epsilon'_{\mathrm{bed}} & \text{in the bed region,} \\ \epsilon_0 & \text{outside the bed region,} \end{cases} \tag{28}$$

where $\epsilon'_{\mathrm{bed}} \geqslant \epsilon_0$. We solve the eigenvalue problem for a range of bed heights h_{bed} and bed permittivities ϵ'_{bed}, where the solutions from the eigenvalue problem together with the corresponding sensitivities are stored in a database. It is noticed that the resonance frequencies and their sensitivities do not change significantly as h_{bed} decreases, if ϵ'_{bed} is increased to an appropriate extent. This is reasonable since it merely corresponds to a redistribution of the bed material to a smaller region. During the evolution of the process, we continuously seek the linearization point ϵ'_{LP} that yields the best fit with the corresponding deviations in the measured resonance frequencies, where the bed height is fixed at a representative value $h_{\mathrm{bed}} = 5$ cm.

Hence, this estimation procedure can be used for a process where the particles grow significantly in size, by means of changing the linearization point ϵ'_{LP}. To summarize, Eq. (25) yields reliable estimates of the perturbations $\delta\epsilon'_{\mathrm{eff}}$ and $\delta\epsilon''_{\mathrm{eff}}$ with respect to the linearization point. This approach is sufficient for most normal process states.

4.1. Sensitivity analysis

The sensitivity analysis is based on the eigensolution $(\boldsymbol{E}_m, \boldsymbol{B}_m, \omega_m)$ computed for a linearization point with $\epsilon'(\boldsymbol{r}) \geqslant \epsilon_0$ and no losses, i.e., $\epsilon''(\boldsymbol{r}) = 0$ and $\sigma(\boldsymbol{r}) = 0$. Given this linearization point, we formulate the sensitivities that relate a small perturbation $\delta\omega_m$ in the resonance frequency ω_m to perturbations in (i) the material parameters $\delta\epsilon'$ and $\delta\epsilon''$ and (ii) the normal displacement δn of the cavity's boundary. Fig. 4a shows a subdivision of the cavity's volume that is used for the parameterization of the material and Fig. 4b shows the cavity's wall with a set of basis functions used for the representation of the normal displacement, where both parameterizations are axisymmetric.

4.1.1. Material sensitivities

Based on the eigenvalue problem (20), the sensitivity of the resonance frequency ω_m with respect to changes in the material parameters $p = \epsilon'$ and ϵ'' is expressed as

$$\frac{\delta\omega_m}{\omega_m} = -\frac{m_{\delta\epsilon'}(\boldsymbol{E}_m, \boldsymbol{E}_m) - jm_{\delta\epsilon''}(\boldsymbol{E}_m, \boldsymbol{E}_m)}{2m_{\epsilon'}(\boldsymbol{E}_m, \boldsymbol{E}_m)}, \tag{29}$$

where we have

$$m_{\delta p}(\boldsymbol{u}, \boldsymbol{v}) = \int_{\Omega} \delta p \boldsymbol{u} \cdot \boldsymbol{v} \, d\Omega, \tag{30}$$

for a perturbation δp with respect to the material parameter p [17,20]. From Eq. (29), we notice that $\delta\epsilon'$ affects only the real part of the eigenfrequencies, and that $\delta\epsilon''$ only affects the imaginary part. The discrete version of this linearization is

$$\frac{\delta\omega_m}{\omega_m} = -\frac{\mathbf{e}_m^{\mathrm{T}}[\mathbf{M}_{\delta\epsilon'} - j\mathbf{M}_{\delta\epsilon''}]\mathbf{e}_m}{2\mathbf{e}_m^{\mathrm{T}}\mathbf{M}_{\epsilon'}\mathbf{e}_m}. \tag{31}$$

4.1.2. Representation of material perturbations

The perturbation δp of the material parameter p is represented in terms of a set of N space dependent basis functions $\varphi_n(\boldsymbol{r})$, which are multiplied with the coefficients δp_n, according to

$$\delta p(\boldsymbol{r}) = \sum_{n=1}^{N} \delta p_n \varphi_n(\boldsymbol{r}). \tag{32}$$

Here, we subdivide the vessel's volume Ω into regions Ω_n such that Ω_n do not overlap and $\bigcup_{n=1}^{N} \Omega_n = \Omega$. We exploit piecewise constant basis functions $\varphi_n(\boldsymbol{r})$ that are equal to one if $\boldsymbol{r} \in \Omega_n$ and zero elsewhere. In particular, we associate the basis functions with three regions: (i) the bed region of height h_{bed} with a relatively high density of particles; (ii) a cylinder shaped volume that coincides with the core of the fountain; and (iii) the rest of the process vessel. These regions are formed by combining the basic subregions shown in Fig. 4a.

The residual $||\mathbf{A}\hat{\mathbf{x}} - \mathbf{b}||$ in the solution to the estimation problem (25) is used as a metric of how well these basis functions are able to represent the actual permittivity

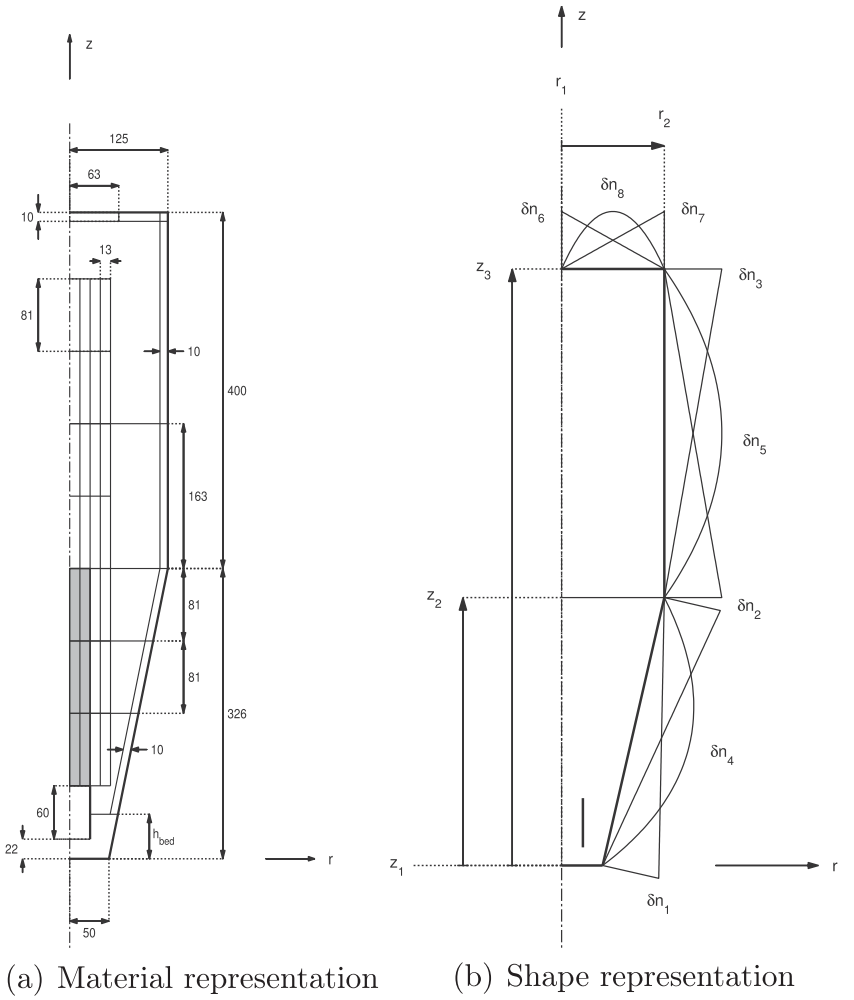

Fig. 4. Two-dimensional projection of the process vessel showing (a) the basic subregions that may be combined in different ways to obtain the material basis functions φ_n and (b) basis functions used to represent shape deformations. All dimensions are in millimeters.

distribution in the experiment. For instance, the height and radius of the fountain region is chosen such that the residual is minimized. Based on measurement results presented later in this article, we find that the fountain region indicated by gray color in Fig. 4a yields the best agreement with the measured resonance frequencies.

4.1.3. Shape sensitivities

For a normal displacement δn of the vessel's boundary Γ, the resulting perturbation in the resonance frequency is given by [17,20]

$$\frac{\delta\omega_m}{\omega_m} = -\frac{d_{\delta n}(\boldsymbol{B}_m, \boldsymbol{B}_m)/\mu_0 - d_{\delta n}(\epsilon' \boldsymbol{E}_m, \boldsymbol{E}_m)}{2W_m}, \tag{33}$$

where W_m is the time-average energy in the cavity given by Eq. (22), and

$$d_{\delta n}(\boldsymbol{u}, \boldsymbol{v}) = \int_\Gamma \boldsymbol{u} \cdot \boldsymbol{v}^* \delta n \, dS. \tag{34}$$

A positive deformation $\delta n > 0$ here corresponds to that the volume of the cavity increases. We notice that shape deformations only affect the real part of the eigenfrequencies.

The corresponding discrete formulation of Eq. (33) is

$$\frac{\delta\omega_m}{\omega_m} = -\frac{\frac{1}{\mu_0}\mathbf{b}^{\mathrm{H}}\mathbf{D}_{\delta n}\mathbf{b} - \mathbf{e}^{\mathrm{H}}\mathbf{D}_{\epsilon'\delta n}\mathbf{e}}{\frac{1}{\mu_0}\mathbf{b}^{\mathrm{H}}\mathbf{M}_1\mathbf{b} + \mathbf{e}^{\mathrm{H}}\mathbf{M}_{\epsilon'}\mathbf{e}}, \tag{35}$$

where the superscript $^{\mathrm{H}}$ indicates conjugate transpose.

4.1.4. Representation of shape perturbations

We use an axisymmetric representation of the normal displacement δn by means of a quadratic hierarchical basis for three different parts of the vessel's boundary: (i) the upper lid; (ii) the cylindrical surface; and (iii) the conical surface. Fig. 4b shows the basis functions in relation to the geometry of the vessel. On each of the three parts of the boundary, we exploit the (local) basis functions

$$\psi_1(u) = 1 - u \tag{36}$$

$$\psi_2(u) = u \tag{37}$$

$$\psi_3(u) = 4u(1-u) \tag{38}$$

where the part of the boundary is parameterized by the local coordinate u such that the interval $0 \leqslant u \leqslant 1$ corresponds to the entire part of the boundary.

In order to constrain the number of degrees of freedom associated with the cavity's shape to a number that is practical, and to suppress non-physical shape deformations, we form two new basis functions by linearly combining $\delta n_1 - \delta n_8$ according to

$$\delta n_{\text{lid}} = 0.97\delta n_6 + 0.24\delta n_8 \tag{39}$$

$$\delta n_{\text{cone/cyl}} = 0.69\delta n_2 + 0.16\delta n_3 + 0.71\delta n_4. \tag{40}$$

Thus, δn_{lid} describes a smooth deformation of the top lid and $\delta n_{\text{cone/cyl}}$ describes a joint deformation of the cylindrical and conical parts of the vessel. The coefficient values in Eqs. (39) and (40) are chosen such that the residual $||\mathbf{A}\hat{\mathbf{x}} - \mathbf{b}||$ is minimized, given only these two independent degrees of freedom for the shape.

4.2. Temperature measurements

Before the vessel is loaded with particles, it is normally pre-heated. We exploit this part of the process to gain information that is used to compute the a priori information $\tilde{\mathbf{x}}$ for later parts of the process. During the pre-heating of the vessel, the vessel is empty and we perform simultaneous and synchronized measurements on (i) the resonance frequencies and (ii) the temperature registered by the set of temperature probes shown in Fig. 2. Given the deviations $\mathbf{y}_{\delta T}$ in the temperatures (relative to the initial temperatures) and the shape perturbations $\hat{\mathbf{x}}_{\delta n}$ estimated from the resonance frequencies for the empty cavity, we use the relatively simple model $\hat{\mathbf{x}}_{\delta n} = \mathbf{B}\mathbf{y}_{\delta T}$, where the matrix $\mathbf{B}$ is determined by means of linear regression from the data acquired during the pre-heating interval. This model is used to obtain a priori estimates $\tilde{\mathbf{x}}_{\delta n} = \mathbf{B}\mathbf{y}_{\delta T}$ from the measured temperatures during later parts of the process, after the particles have been loaded. In the following, we exploit the a priori information

$$\tilde{\mathbf{x}} = \begin{bmatrix} \tilde{\mathbf{x}}_{\delta\epsilon_{\text{eff}}} \\ \tilde{\mathbf{x}}_{\delta n} \end{bmatrix} = \begin{bmatrix} 0 \\ \mathbf{B}\mathbf{y}_{\delta T} \end{bmatrix}, \tag{41}$$

in the estimation problem (25), where $\tilde{\mathbf{x}}_{\delta\epsilon_{\text{eff}}}$ corresponds to all the material parameters that are incorporated in the estimation procedure.

Tests demonstrate that about 95% of the perturbations in the resonance frequencies due to thermal expansion of the vessel during heating and cooling can be accounted for by this model, when the vessel is empty. This approach is less successful once the vessel is loaded with particles, since the presence of particles yields a different temperature distribution in the vessel. However, it is presumed that it is feasible to improve the a priori information, should the metal temperature be measured at more places on the vessel's wall and top lid.

5. Results

In the measurement results presented in the following, we perform repeated microwave measurements on the process vessel as the process is running. Each process experiment typically takes a few hours in total. The external process parameters such as the flow-rate, temperature and humidity of the fluidizing air, the pressure and flow in the pneumatic spray-nozzle and the flow-rate of the spraying liquid, are controlled from the user interface of the process machine. These external process parameters together with measured temperatures at the locations indicated in Fig. 2, are logged by the process machine.

5.1. Cavity without particles

Among the eigenmodes hosted by the process vessel we have identified eight modes that are feasible to use for sensing. These modes are listed in Table 1 together with their resonance frequencies and unloaded Q-values. All these modes have similarities with the TE and TM modes hosted by a circular cylindrical cavity. In particular, the modes $m = 1, 2, 5$ and 7 resemble the modes $\text{TE}_{111}, \text{TE}_{112}, \text{TE}_{113}$, and TE_{114} of a circular cylindrical cavity, and the modes $m = 3, 4$ and 6 resemble the modes $\text{TM}_{010}, \text{TM}_{011}$ and TM_{012} respectively. The mode $m = 7$ (TE_{114}) has a strong electric field in the lower part of the vessel, which makes it well-suited for probing the permittivity in the down-bed region. The mode $m = 8$ resembles TE_{011} which has an electric field that is zero on all cavity walls, which implies that its resonance frequency is insensitive to dielectric material adhering to the cavity walls. This mode also has a notably high Q-value.

The loaded Q-values in the experiment can be calculated from the real and imaginary part of the measured complex resonance frequency ω according to

$$Q_{\text{l}} = \frac{\text{Re}(\omega)}{2 \cdot \text{Im}(\omega)}, \tag{42}$$

for the weakly damped cavity modes [17]. Since the cavity is loaded by two probes with different coupling coefficients, the following expression is used to calculate the unloaded Q-value

$$Q_{\text{u}} = Q_{\text{l}}\left(\frac{2}{|S_{11}| + |S_{22}|}\right), \tag{43}$$

where the reflection coefficients S_{11} and S_{22} are evaluated at each resonance frequency [21].

We calculate the Q-value from the electromagnetic model using the method described in Section 3.3, and here we assume that the cavity walls have a conductivity $\sigma_{\text{c}} = 10^6$ S/m, which should be representative for the stainless steel that the vessel is made of.

Table 1
Computed and measured values of the resonance frequencies and unloaded Q-values of the lowest eigenmodes in the process vessel. The variabilities (here represented by one standard deviation) in the measured quantities arise from disassembling and reassembling the complete vessel.

m	Computed		Measured	
	f_0 (MHz)	Q	f_0 (MHz)	Q
1	759	5100	761 ± 0.07	5400 ± 100
2	894	5800	894 ± 0.05	5100 ± 400
3	928	5900	930 ± 0.02	4400 ± 400
4	1008	6000	1009 ± 0.03	3200 ± 800
5	1051	6100	1051 ± 0.06	4700 ± 200
6	1149	6300	1150 ± 0.03	3400 ± 700
7	1207	5600	1206 ± 0.08	3500 ± 300
8	1495	9800	1498 ± 0.05	10,300 ± 400

As can be seen in Table 1, the measured and computed resonance frequencies agree well. There is also a generally good agreement between measured and computed Q-values although, for some modes, the measured Q-value is significantly lower than the computed. The latter may be a result of insufficient electric contact in the joint between the conical and cylindrical part of the cavity, or at the aluminum foil that covers the windows. As the process vessel is disassembled and reassembled, a certain variability in the measured resonance frequencies and Q-values is introduced, which is presented in Table 1. This variability is significant in relation to the perturbations in resonance frequencies caused by changes in the state of the process. Therefore, the particles are inserted into the process vessel through a small hole (indicated by H1 in Fig. 2) after the necessary reference measurements on the empty cavity have been collected, in order to eliminate this variability. Investigations show that the variability introduced from inserting the particles in this manner is negligible.

5.1.1. Effects from air humidity and spray

In a Wurster-process, several different components that influence the resonance frequencies are present simultaneously. The most important of these components are (i) particles, (ii) the temperature of the vessel (iii) liquid droplets from the spray nozzle and (iv) water vapor in the fluidizing air. The temperature of the vessel affects the resonance frequencies mainly via perturbations of the cavity's shape, whereas the other components are assumed to influence the resonance frequencies via the permittivity. In order to assess how each of these components contribute to the microwave response, they have been studied separately. Some of these components, such as the spraying liquid and the temperature, are inherently interconnected, i.e., the spraying rate cannot be changed without also affecting the temperature.

The humidity of the fluidizing air can be controlled independently using the process machine and humidities ranging from 0 to 20 (g H_20)/(kg air), corresponding to dew-points in the range from -30 °C to 25 °C, can be achieved. Our measurements show that the humidity influences only the real part of the permittivity of the air and hence the resonance frequencies, to a degree that is clearly detectable.

Water sprayed from the pneumatic spray nozzle (also referred to as the atomizer) yields similar changes in the permittivity inside the cavity as the humidity does. Only ϵ'_{eff} is influenced by the spray, and if the same amount of water is added through the atomizer as via the fluidizing air, the change in ϵ'_{eff} is very similar. The contributions to the permittivity of the air from humidity in the fluidizing air and from water spray are additive, as long as the spraying rate is sufficiently low to allow for complete evaporation of the liquid droplets.

5.2. Measurements with particles

In the following, we present measurement results for processes involving particles. The particles used are made of MCC (Cellets® brand) and have diameters in a distribution from 500 to 700 μm. A batch consisting of 200 g of particles is used in all of the following experiments. All process settings are identical in the following experiments, except for the type of spraying solution and the spraying rate. The fluidization flow is set to 30 Nm^3/h (where N denotes normal temperature and pressure) with an inlet temperature of 70 °C. The atomizer pressure is 2.0 bar and the associated atomizer flow is 2.0 Nm^3/h.

The spraying liquid used in the experiments is water containing either (i) Mannitol or (ii) NaCl. The permittivity of these spraying liquids is measured using the dielectric probe kit 85070E from Agilent Technologies, and the results are shown in Fig. 5.

In the beginning of each experiment, the vessel is preheated and the particles are loaded, before the experiment-specific part of the process (e.g. coating) is initiated. In the results presented in the following, we omit the preheating interval and focus on the experiment-specific parts.

The average error between the model and measurement is computed as the root-mean-square of the difference between measurements ($\mathbf{b}$) and model fit ($\mathbf{A}\hat{\mathbf{x}}$), averaged with respect to the number of sensing modes M. With particles present in the vessel, this average error is in the order of 10^{-5} during normal process conditions (no extensive agglomeration, etc.) which should be compared with the average magnitude of the measurement response ($||\mathbf{b}||/M$), which is in the order of 10^{-3}.

According to the sensitivity analysis in Section 4.1, perturbations in the real part of the resonance frequencies are related to both $\delta\epsilon'_{\text{eff}}$ and δn. Similarly, a perturbation in the imaginary part of the resonance frequency is related to $\delta\epsilon''_{\text{eff}}$. As described in Section 4.2, δn is to a large extent determined based on a priori information that exploits temperature measurements. An error in the a priori information may yield a corresponding error in $\delta\epsilon'_{\text{eff}}$, which varies on a timescale that is significantly slower than the fast timescales associated with the fluid-dynamics of the process. Based on these two time-scales, we make the assumption $\epsilon_{\text{eff}}(t) = \epsilon_{\text{eff,slow}}(t) + \epsilon_{\text{eff,fast}}(t)$, where $\epsilon_{\text{eff,fast}}(t)$ represents fast random fluctuations and $\epsilon_{\text{eff,slow}}(t)$ represents slow changes in the permittivity caused either by errors in the a priori information or by changes in the actual process state (such as particles growing in size or accumulation of moisture in the particles). We model $\epsilon_{\text{eff,slow}}(t)$ by a low-order polynomial with respect to time t, and this polynomial is determined by means of linear regression based on the estimated $\epsilon_{\text{eff}}(t)$. Furthermore, we compute the covariance matrix from the real and imaginary part of $\epsilon_{\text{eff,fast}}(t)$ according to $\mathbf{C} = \text{cov}(\mathbf{z}_1, \mathbf{z}_2)$ where $\mathbf{z}_1 = [\epsilon'_{\text{eff,fast}}(t_n)/\epsilon_0 - 1]^{\text{T}}$ and $\mathbf{z}_2 = [\epsilon''_{\text{eff,fast}}(t_n)/\epsilon_0]^{\text{T}}$ are vectors containing samples of $\epsilon_{\text{eff,fast}}$ taken at discrete time instants t_n. If the eigenvectors of $\mathbf{C}$ are scaled by the square root of its eigenvalues (i.e. the standard deviations), they define the major and minor semi-axes of an ellipse that represent the co-variation of the data. Such ellipses are included in the scatter-plots in the presentation of the following measurement results. Variations in $\epsilon_{\text{eff,fast}}(t)$ along the eigenvector associated with the largest eigenvalue of $\mathbf{C}$, are mainly attributed to fluctuations in the particle volume fraction ϑ. Therefore, we take the slope of this eigenvector (i.e. the major semi-axis of the ellipse) as a density-independent ratio which is equivalent to the ratio η in Section 2.2.2.

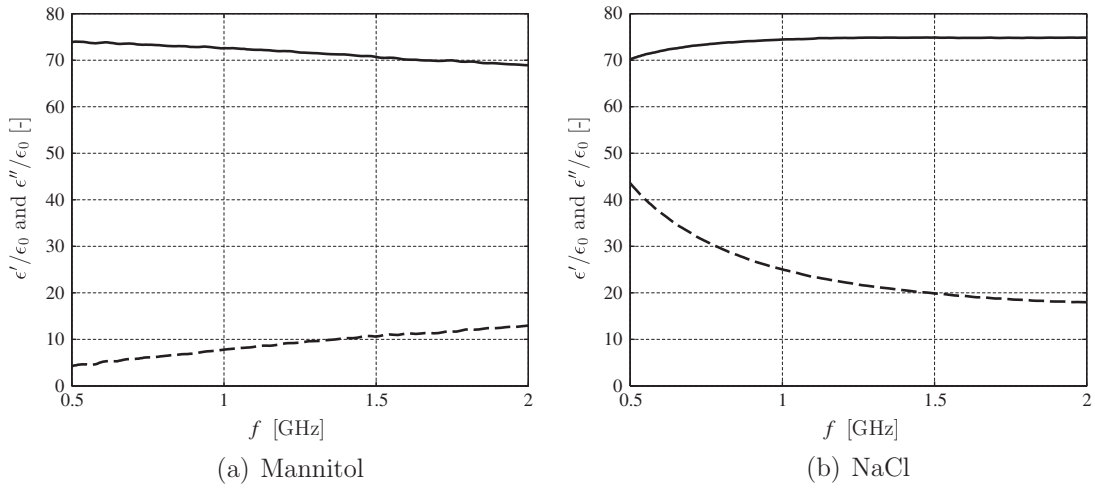

Fig. 5. Relative permittivity of distilled water at room temperature that contains (a) Mannitol (13.5%) and Kollicoat IR® (1.5%), and (b) NaCl (0.5%). Solid curves represent ϵ'/ϵ_0 and dashed curves ϵ''/ϵ_0.

The relationship between this slope and underlying physical parameters such as the moisture content of the particles and the concentration of salt (NaCl) in the spraying liquid, have been studied by means of Monte-Carlo simulations. These simulations are based on measurements of the complex permittivity of MCC [11] and empirical models for the permittivity of water with and without salt [10], together with the mixing formulas described in Section 2.2.1. Thus, we generate random mixtures of MCC particles and air by using statistical normal-distributions to represent the volume fraction and water content of the particles. The water is assumed to be either absorbed uniformly in the MCC-particles or distributed in a uniform water-layer on the surface of the particles. The case with a pronounced water-layer may be representative also for situations where the surface of the particles have a substantially higher moisture content than the core. Based on these simulations, we observe the following trends:

1. An increase in the moisture content of the MCC particles (absorbed water) *increases* the slope, if the initial moisture content is less than around 7%. For higher moisture contents, the slope instead *decreases* with increasing moisture content.
2. Pure water distributed on the surface of the particles *decreases* the slope.
3. Water containing salt distributed on the surface of the particles *increases* the slope if the salt concentration exceeds 1%.
4. The slope is *not* affected by changes in the volume fraction, if the volume fraction is sufficiently low (around 5% or lower), whereas at higher volume fractions, the slope *increases* with increasing volume fraction.

5.2.1. Fast coating process

Here, we present results from a process where MCC particles are coated with a mixture of Mannitol (a sugar) and a polymer labeled Kollicoat IR® (ethylene glycol vinyl acetate grafted polymer), where the Mannitol and the Kollicoat IR are dissolved in de-ionized water. The dry content of the solution (the fraction that ideally stays on the surface of the particles) is 15 mass% (13.5% Mannitol and 1.5% Kollicoat IR). The complex relative permittivity for this solution is shown in Fig. 5a, and here we notice that the response is similar to that of pure water. In this experiment, a relatively high spraying rate is used to obtain fast build-up of the coating layer. First, the spraying rate is set to 11.3 g/min and kept constant during approximately 15 min. Next, the spraying rate is increased even further to 14.4 g/min, which eventually leads to extensive agglomeration and particles adhering to the walls of the vessel.

Fig. 6 shows the estimated permittivity in three different regions: (i) the down-bed region; (ii) the fountain region above the Wurster tube; and (iii) the rest of the volume above the down-bed region, as function of process time in hours. At $t = 0.9$ h, the particles are fluidized in the process with the fountain off, and the temperature is in equilibrium. The following changes in process settings are marked with dashed vertical lines: at $t = 1.04$ h the fountain is switched on; in the interval $1.2\text{ h} < t < 1.26$ h the spraying rate is successively increased to 11.3 g/min; at $t = 1.51$ h the spraying rate is increased to 14.4 g/min. Some interesting features can be observed in these figures:

1. The estimated permittivities fluctuate substantially, which is reasonably caused by the continuous redistribution of the particles in the process which occurs on a short time scale (<0.1 s).
2. As the fountain is switched on, the estimated permittivity increases clearly in the fountain and remaining volume regions, whereas it decreases in the bed region. This is reasonable since as the fountain is switched on, particles start to circulate in the upper part of the vessel which reduces the amount of particles in the down-bed region.
3. The estimated permittivity in the fountain decreases slightly as the spraying starts. This could be an artifact (incorrect estimation) resulting from insufficient

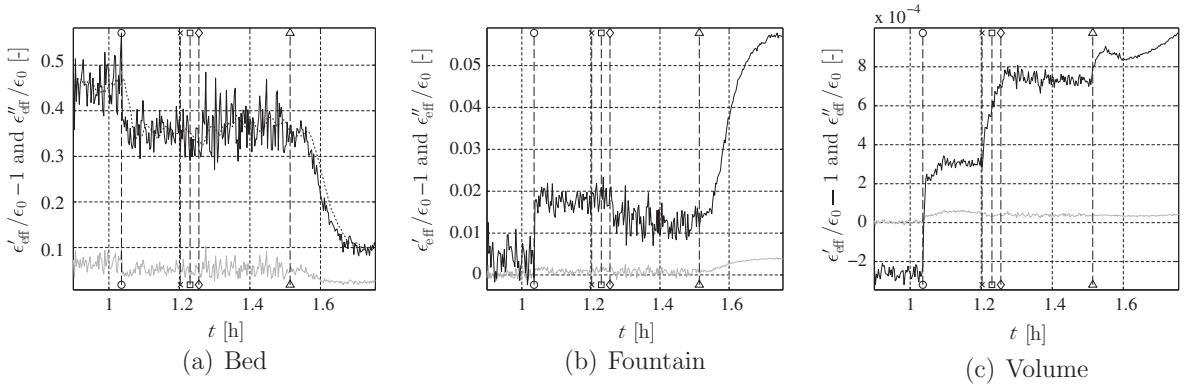

Fig. 6. Estimated permittivity as a function of process time in the fast coating process. Black lines represent $\epsilon'_{\rm eff}/\epsilon_0 - 1$ and gray lines $\epsilon''_{\rm eff}/\epsilon_0$. The dashed black curve in (a) shows the permittivity in the bed region at the current linearization point.

compensation for temperature variations, but it could also be due to a lower particle density in the fountain as the spraying starts. The estimated permittivity in the remaining volume increases as the spraying starts, reasonably due to increased air humidity inside the vessel.

4. During the interval 1.5 h < t < 1.75 h, extensive agglomeration occurs in the process and the particles start to build up dense layers on parts of the cavity walls, as a result of the high spraying rate (this could be observed visually after the experiment was finished). This process is clearly reflected in the estimated permittivities, which are changing dramatically during the agglomeration interval.

In situations similar to the agglomeration interval described in item 4 above, i.e. at very moist process conditions that yields material build-up on the vessel walls, we repeatedly observe a larger discrepancy between the model and measurements, i.e. an increasing residual $||\mathbf{A}\hat{\mathbf{x}} - \mathbf{b}||$. Thus, a model that allows only for a constant permittivity in the bed, fountain and remaining volume regions, is unable to accurately represent the material distributions formed during extensive agglomeration. This indicates the possibility of detecting anomalous process conditions based on the residual. Studies show however that it is possible to maintain a low residual also during extensive agglomeration if the cavity is divided into sub-regions that better represent the actual material distribution. The sub-regions in the direct vicinity of the cavity walls shown in Fig. 4a may be well-suited for this purpose.

Fig. 7 shows scatter plots of $\epsilon''_{\rm eff}/\epsilon_0$ versus $\epsilon'_{\rm eff}/\epsilon_0 - 1$ in the three regions before and after spraying starts. The ellipses in these scatter plots represent the co-variation of the data, where the length of each semi-axis is three standard deviations. All ellipses are highly elongated and the variations along the major semi-axis is assumed to be caused by variations in material density, according to the discussion on density-independent functions in Section 2.2.2. The slopes in the scatter plots are shown in Table 2. Here we notice that (i) the slope is higher in the bed region, as compared to the fountain and volume regions and (ii) the slope decreases in the fountain and in the volume after the spraying starts, but remain unchanged in the bed. According to the results from the Monte-Carlo simulations described previously, the decreasing slope in the fountain and volume regions could indicate that the moisture content at the surface of these particles increases during the spraying interval. The higher slope in the bed is in agreement with the Monte-Carlo simulations, since the volume fraction in the bed is substantially higher than in the other regions.

5.2.2. Slow coating process

In this experiment, MCC particles are coated with Mannitol and Kollicoat IR® with the mixing ratio described in Section 5.2.1, under relatively dry process conditions, i.e., a relatively low spraying rate of 6.6 g/ min is used.

Fig. 8 shows the estimated permittivity in the bed, fountain and remaining volume regions, as function of process time in hours. The time interval 0 h < t < 0.9 h, which has been omitted, includes pre-heating of the vessel and loading of particles, so at t = 0.9 h, the particle fountain is switched on and the temperature is close to equilibrium. The process conditions are changed at the time instants indicated by the dashed vertical lines: at t = 0.89 h spraying (coating) starts with a spraying rate of 4.6 g/min; at t = 0.96 h the spraying rate is increased to the final value 6.6 g/min; at t = 1.13 h the temperature is considered stable and at t = 1.78 h the spraying ends. In these figures, some interesting features can be observed:

1. The estimated permittivity in the bed increases slowly during the coating interval 0.90 h < t < 1.78 h, whereas the permittivities in the fountain and the remaining volume regions remain fairly constant. This may be explained by particles growing in size as a result of the coating, which results in more dielectric material that accumulates mainly in the bed region. The growth in particle size was verified by means of sieving and weighing the particles after the coating process was finished, and the mass-increase was found to be approximately 25%. A bed that grows in size in the experiment is interpreted by our model as an increase in the effective permittivity in the bed-region, which has a fixed size. This effect can however not be clearly

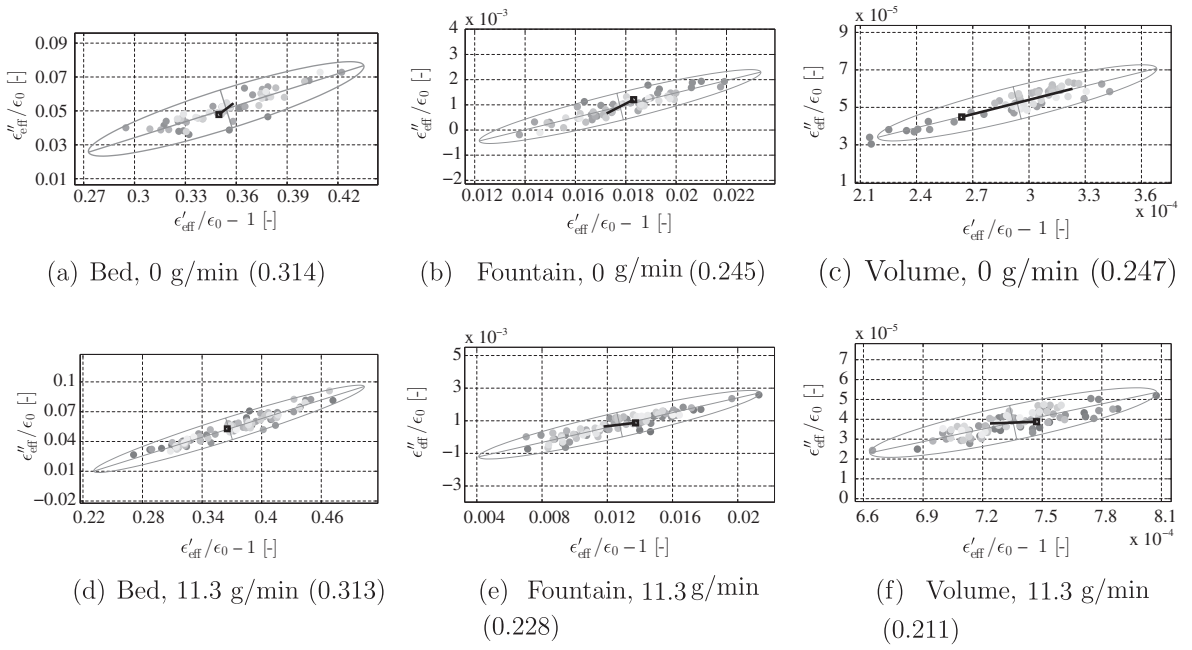

Fig. 7. Scatter plots of $\epsilon''_{\text{eff}}/\epsilon_0$ versus $\epsilon'_{\text{eff}}/\epsilon_0 - 1$ in the fast coating process. Values inside parentheses are the slopes of the major semi-axis of the ellipses. The black lines starting with squares represent the slowly varying component $\epsilon_{\text{eff,slow}}$ of the estimated permittivity.

Table 2
Slopes of the major semi-axis in the scatter plots of ϵ''_{eff} versus $\epsilon'_{\text{eff}} - 1$.

	Bed	Fountain	Volume
Spraying off	0.314	0.245	0.247
Spraying 11.3 g/min	0.313	0.228	0.211

observed in the fast coating experiment described in Section 5.2.1, which is somewhat surprising given that we use the same coating solution in both processes.

2. The permittivity in the remaining volume region (Fig. 8) increases as the spraying starts, it increases further as the spraying rate increases and drops as the spraying is stopped. This may be attributed to changes in the permittivity of the air, due to increased humidity caused by the evaporating water in the spray.

Fig. 9 shows scatter plots of $\epsilon''_{\text{eff}}/\epsilon_0$ versus $\epsilon'_{\text{eff}}/\epsilon_0 - 1$ for the tree regions, during the coating interval. Here, we notice that the slope is higher in the bed as compared to the other two regions, which is reasonable given the higher volume fraction in the bed. We also notice how the slowly varying component $\epsilon_{\text{eff,slow}}$ shown by black lines in Fig. 9, varies substantially in the bed region, reasonably due to the growth in particle size.

5.2.3. Particles sprayed with salt water

In this experiment, MCC particles are sprayed with salt water (0.5 mass% NaCl dissolved in distilled water at room temperature). The complex relative permittivity for this solution is shown in Fig. 5b and here we notice a significant increase in ϵ'' at low frequencies due to the conductivity

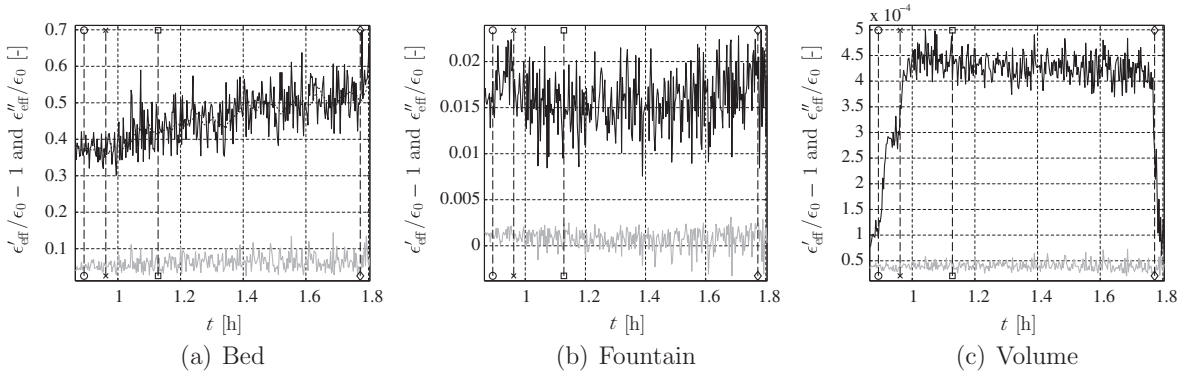

Fig. 8. Estimated permittivity as a function of process time in the slow coating process. Black curves represent $\epsilon'_{\text{eff}}/\epsilon_0 - 1$ and gray curves $\epsilon''_{\text{eff}}/\epsilon_0$. The dashed black curve in (a) shows the permittivity in the bed region at the current linearization point.

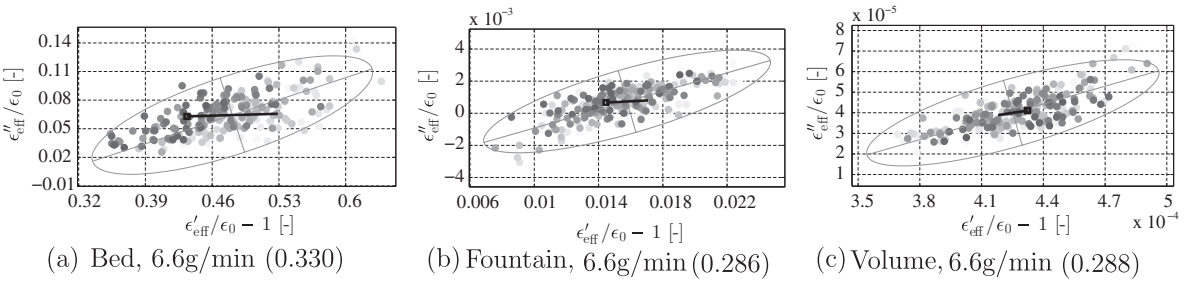

Fig. 9. Scatter plots of $\epsilon''_{\text{eff}}/\epsilon_0$ versus $\epsilon'_{\text{eff}}/\epsilon_0 - 1$ in the slow coating process. Values inside parentheses are the slopes of the major semi-axis of the ellipses. The black lines starting with squares represent $\epsilon_{\text{eff,slow}}$, i.e. the slowly varying component of the estimated permittivity.

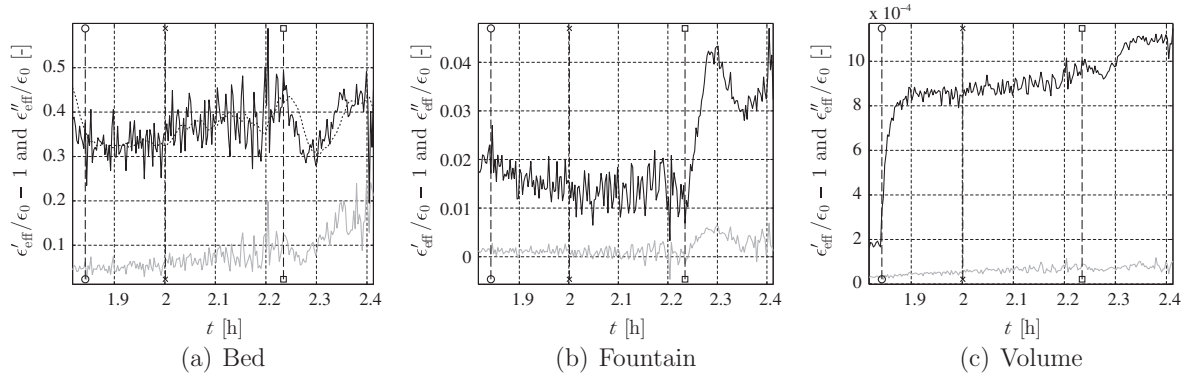

Fig. 10. Estimated permittivity as a function of process time in the salt water experiment. Black curves represent $\epsilon'_{\text{eff}}/\epsilon_0 - 1$ and gray curves $\epsilon''_{\text{eff}}/\epsilon_0$. The dashed black curve in (a) shows the permittivity in the bed region at the current linearization point.

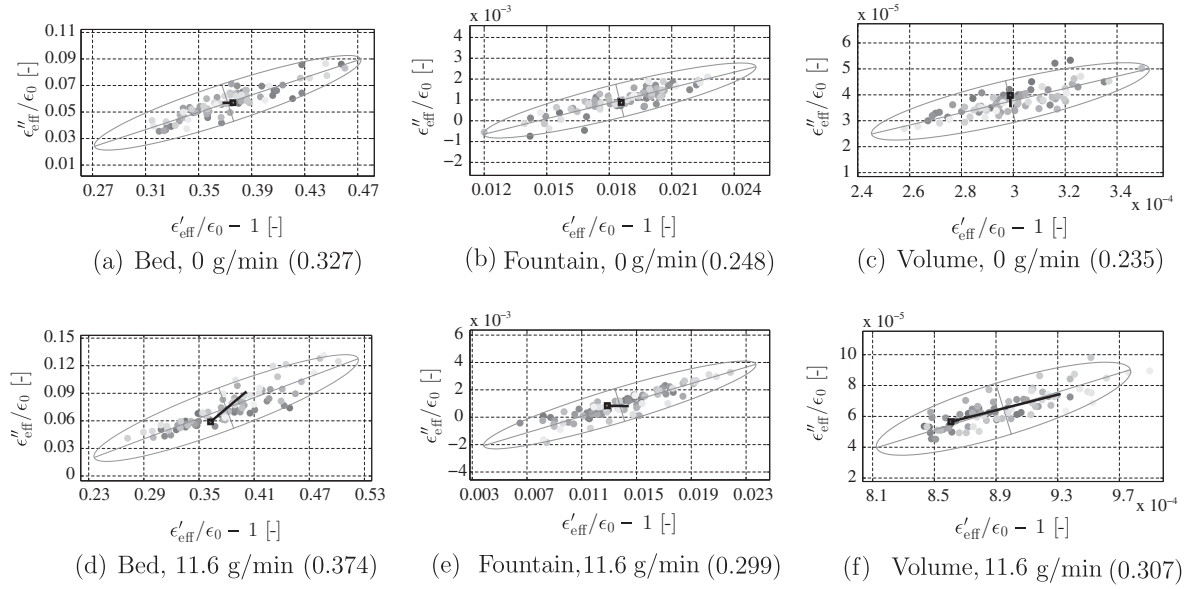

Fig. 11. Scatter plots of $\epsilon''_{\text{eff}}/\epsilon_0$ versus $\epsilon'_{\text{eff}}/\epsilon_0 - 1$ in the salt water experiment. Values inside parentheses are the slopes of the major semi-axis of the ellipses. The black lines starting with squares represent the slowly varying component $\epsilon_{\text{eff,slow}}$ of the estimated permittivity.

introduced by the salt. Two different spraying rates are studied, namely 11.6 g/ min and 13.3 g/ min.

Fig. 10 shows the estimated permittivity in the bed, fountain and remaining volume regions, as function of process time in hours. At the first time instant shown in Fig. 10, the particles are fluidized, the fountain is on and the temperature is stable. The following changes in process settings are marked with dashed vertical lines: at t = 1.84 h

Table 3
Slopes of the major semi-axis in the scatter plots of ϵ''_{eff} versus $\epsilon'_{\text{eff}} - 1$ for the salt water experiment.

	Bed	Fountain	Volume
Spraying off	0.327	0.248	0.235
Spraying: 11.6 g/min	0.374	0.299	0.307

the spraying starts (11.6 g/min); at $t = 2$ h the temperature is considered stable; at $t = 2.24$ h the spraying rate is increased to 13.3 g/min which yields very moist process conditions and presumed initiation of extensive agglomeration. The increase in spraying rate to 13.3 g/min is followed by clear changes in the estimated permittivities, possibly due to free water (with salt) on the surface of the particles in the fountain region and/or agglomeration with particles adhering to the walls of the vessel.

Fig. 11 shows scatter plots of $\epsilon''_{\text{eff}}/\epsilon_0$ versus $\epsilon'_{\text{eff}}/\epsilon_0 - 1$ in two intervals: (i) no spray and (ii) spraying at 11.6 g/min (which does *not* yield agglomeration). The slopes of the major axis for the three regions is also presented in Table 3. Here, it is interesting to notice how the slopes in all regions clearly increase after the spraying is switched on. This is expected, given the high dielectric losses of the salt water in the frequency range of the cavity resonances, and it is also in agreement with the Monte-Carlo simulations presented previously.

6. Conclusions

We have presented a microwave measurement technique for industrial processes contained in closed metal vessels, which exploits a number of electromagnetic resonances of the metal vessel to estimate the process state. In particular, we estimate the effective permittivity inside a vessel that hosts a pharmaceutical fluidized-bed process, which is used for particle coating. This process involves spraying a solution onto the particles, where water acts as the solvent for different types of coating substances. For this particular application, it is important to monitor the moisture content of the particles and the particle distribution. Electromagnetic waves interact strongly with water in a non-invasive and non-destructive manner, which makes this type of measurement technology very attractive. In addition, our measurement system is sensitive to changes in permittivity throughout the process vessel and, thus, it can be considered to perform a global measurement of the process state, which is challenging for more conventional techniques.

We exploit two magnetic field probes and measure the scattering parameters as function of frequency using a network analyzer. The complex resonance frequencies are estimated from the scattering parameters and these are related to a reference measurement of the empty vessel in order to achieve relative changes in the resonance frequencies. The perturbations in the resonance frequencies are related to (i) the perturbations in the complex effective permittivity inside the vessel and (ii) the thermal expansion of the vessel caused by variations in the temperature. We exploit an estimation algorithm with regularization to estimate the effective permittivity and the shape of the vessel, where the unknown effective permittivity and shape is parameterized with the aid of spatial basis functions. The real and imaginary part of the effective permittivity are assumed to be frequency-independent in the frequency band of the used resonance frequencies. We model the vessel by means of the finite element method and the computed eigenmodes and eigenfrequencies are used to calculate sensitivities with respect to changes in the material parameters and the shape of the vessel. The estimation incorporates a priori information that is collected from probes that measure the temperature of the vessel's metal walls and the air that flows through the vessel. This approach accounts for substantial parts of the temperature variations but it is believed that it can be significantly improved.

The measurement technique performs well for the estimation of the effective permittivity that is parameterized for a small number of sub-regions. The re-distribution of material occurring when the particle fountain is switched on, is clearly reflected in the estimated permittivity in all these sub-regions. The effect of particles that grow in size during coating processes can be observed in the estimated permittivities, and we have also shown that material build-up on the cavity walls can be clearly detected. We have related the real part of the effective permittivity to its imaginary part by means of scatter plots and covariance matrices, where measurements taken at different time instants fall approximately on a straight line. This line is defined by the eigenvector associated with the largest eigenvalue of the covariance matrix, and the slope of the line is affected by the liquid sprayed onto the particles in the process. In particular, the slope of this line clearly increases if the particles are sprayed with a liquid that features substantial dielectric losses.

Acknowledgements

Livia Cerullo was financially supported by AstraZeneca. In addition, Johan Winges was financially supported by the Swedish Research Council (dnr 2010-4627) in the project "Model-based Reconstruction and Classification Based on Near-Field Microwave Measurements". The computations were performed on resources at Chalmers Centre for Computational Science and Engineering (C3SE) provided by the Swedish National Infrastructure for Computing (SNIC).

References

[1] J. Rantanen, S. Lehtola, P. Rämet, J.-P. Mannermaa, J. Yliruusi, On-line monitoring of moisture content in an instrumented fluidized bed granulator with a multi-channel NIR moisture sensor, Powder Technol. 99 (1998) 163–170.
[2] T.D. Beer, A. Burggraeve, M. Fonteyne, L. Saerens, J. Remon, C. Vervaet, Near infrared and Raman spectroscopy for the in-process monitoring of pharmaceutical production processes, Int. J. Pharm. 417 (2011) 32–47.
[3] C. Buschmüller, W. Wiedey, C. Döscher, J. Dressler, J. Breitkreutz, In-line monitoring of granule moisture in fluidized-bed dryers using microwave resonance technology, Euro. J. Pharm. Biopharm. 69 (2008) 380–387.
[4] V. Rimpiläinen, L.M. Heikkinen, M. Vauhkonen, Moisture distribution and hydrodynamics of wet granules during fluidized-bed drying

characterized with volumetric electrical capacitance tomography, Chem. Eng. Sci. 75 (2012) 220–234.
[5] M. Dressel, O. Klein, S. Donovan, G. Grüner, Microwave cavity perturbation technique: Part III: applications, Int. J. Infrared Millimeter Waves 14 (1993) 2489–2517.
[6] B. Meng, J. Booske, R. Cooper, Extended cavity perturbation technique to determine the complex permittivity of dielectric materials, IEEE Trans. Microwave Theory Tech. 43 (1995) 2633–2636.
[7] S. Karlsson, A. Rasmuson, B. van Wachem, I.N. Björn, CFD modeling of the Wurster bed coater, AIChE J. 55 (2009) 2578–2590.
[8] A. Sihvola, Electromagnetic Mixing Formulas and Applications, The Institution of Engineering and Technology (2008).
[9] G. Kristensson, S. Rikte, A. Sihvola, Mixing formulas in the time domain, J. Opt. Soc. Am. 15 (1998) 1411–1422.
[10] E. Nyfors, P. Vainikainen, Industrial Microwave Sensors, Artech House, 1989.
[11] L. Gradinarsky, H. Brage, B. Lagerholm, I.N. Björn, S. Folestad, In situ monitoring and control of moisture content in pharmaceutical powder processes using an open-ended coaxial probe, Measure. Sci. Technol. 17 (2006) 1847–1853.
[12] S. Trabelsi, S.O. Nelson, Density-independent functions for on-line microwave moisture meters: a general discussion, Measure. Sci. Technol. 9 (1998) 570–578.
[13] D.A. Engers, M.N. Fricke, R.P. Storey, A.W. Newman, K.R. Morris, Triboelectrification of pharmaceutically relevant powders during low-shear tumble blending, J. Electrostat. 64 (2006) 826–835.
[14] D.A. Engers, M.N. Fricke, A.W. Newman, K.R. Morris, Triboelectric charging and dielectric properties of pharmaceutically relevant mixtures, J. Electrostat. 65 (2007) 571–581.
[15] J.C. Nédélec, Mixed finite elements in $\mathbb{R}^3$, Numer. Math. 35 (3) (1980) 315–341.
[16] T. Rylander, A. Bondeson, P. Ingelström, Computational Electromagnetics, Springer, 2012.
[17] D. Pozar, Microwave Engineering, second ed., Wiley, 1998.
[18] T. McKelvey, H. Akçay, L. Ljung, Subspace-based multivariable system identification from frequency response data, IEEE Trans. Automatic Control 41 (1996) 960–979.
[19] S.M. Kay, Fundamentals of Statistical Signal Processing: Estimation Theory, Prentice Hall, 1993.
[20] I.W. Lee, D.O. Kim, G.H. Jung, Natural frequency, Natural frequency and mode shape sensitivities of damped systems: Part I, distinct natural frequencies, J. Sound Vib. 223 (1999) 399–412.
[21] K. Leong, J. Mazierska, Measurements of unloaded Q-factor of transmission mode dielectric resonators, in: IEEE MTT-S International Microwave Symposium Digest 3, 1997.